COMMUNICATION

ADVANCED
MATERIALS
www.advmat.d

Check for
updates

Deep-Blue Perovskite Single-Mode Lasing through Efficient Vapor-Assisted Chlorination

Joao M. Pina, Darshan H. Parmar, Golam Bappi, Chun Zhou, Hitarth Choubisa, Maral Vafaie, Amin M. Najarian, Koen Bertens, Laxmi Kishore Sagar, Yitong Dong, Yuan Gao, Sjoerd Hoogland, Makhsud I. Saidaminov, and Edward H. Sargent*

Metal halide perovskites have emerged as promising candidates for solution-processed laser gain materials, with impressive performance in the green and red spectral regions. Despite exciting progress, deep-blue—an important wavelength for laser applications—remains underexplored; indeed, cavity integration and single-mode lasing from large-bandgap perovskites have yet to be achieved. Here, a vapor-assisted chlorination strategy that enables synthesis of low-dimensional $CsPbCl_3$ thin films exhibiting deep-blue emission is reported. Using this approach, high-quality perovskite thin films having a low surface roughness (RMS ≈ 1.3 nm) and efficient charge transfer properties are achieved. These enable us to document low-threshold amplified spontaneous emission. Levering the high quality of the gain medium, vertical-cavity surface-emitting lasers with a low lasing threshold of 6.5 µJ cm^{-2} are fabricated. This report of deep-blue perovskite single-mode lasing showcases the prospect of increasing the range of deep-blue laser sources.

The active gain medium of a semiconductor laser diode is often comprised of a multiple quantum well (QW) structure grown through expensive epitaxial methods such as chemical vapor deposition or molecular beam epitaxy.[1] These layered heterostructures provide carrier and electromagnetic field confinement because of bandgap and refractive index contrast between the quantum well and the surrounding cladding layers, leading

to decreased thresholds and improved laser action.[1,2]

Reduced-dimensional metal halide perovskites (RDPs) are self-assembled solution-based natural quantum wells with the chemical formula of $A'_2A_{n-1}M_nX_{3n+1}$, with A' commonly being a long organic cation (such as $C_4H_{12}N^+$ [BA$^+$] and $C_8H_{12}N^+$ [PEA$^+$]), A a smaller size cation (such as $CH_3NH_3^+$ [MA$^+$] and Cs$^+$), M a divalent metal cation (such as Pb^{2+} and Sn^{2+}), and X a halide (Cl$^-$, Br$^-$, or I$^-$).[3–5] The large A' organic molecule, usually long-chain aliphatic or aromatic alkylammonium cations, provides the large bandgap, low permittivity, and low refractive index to achieve the contrast required to confine generated excitons and electromagnetic field within the inorganic octahedral cages composing the perovskite.

As in epitaxially grown QWs, solution-based RDPs achieve increased exciton binding energy and overall optical oscillator strengths.[4,6] The degree of exciton confinement within the well is determined by the number (*n*) of octahedral monolayers enclosed by the large organic cations. The contrasting bandgap and band alignment between the different wells provides an energy gradient which leads to charge transfer toward smaller bandgap domains.[7,8] The hydrophobic nature of the A' cation improves the overall device stability under ambient conditions, increasing the viability of the material as a candidate for optoelectronic applications.[9] Stronger optical oscillator strength, faster population inversion via energy transfer along quantum wells, and improved stability make RDPs attractive solutions for laser devices.

Laser action and amplified spontaneous emission (ASE) using RDPs as an active gain media have been demonstrated in the green and red spectral regions.[3–5,10,11] Fast energy transfer along quantum wells concentrates photogenerated carriers in the lowest-bandgap domain, leading to fast population inversion and stimulated emission. This leads to gain coefficients in RDPs exceeding those of their 3D counterparts,[3,5] and stable laser action for more than 10 h.[4,5] However, cavity integration and lasing from large-bandgap RDPs have not been achieved even though deep-blue lasing emission is of considerable interest in lithography, high-density data storage, and medical and scientific devices. Reports of deep-blue perovskite

J. M. Pina, D. H. Parmar, G. Bappi, C. Zhou, H. Choubisa, M. Vafaie,
Dr. A. M. Najarian, K. Bertens, Dr. L. K. Sagar, Dr. Y. Dong, Prof. Y. Gao,
Dr. S. Hoogland, Prof. M. I. Saidaminov,[+] Prof. E. H. Sargent
The Edward S. Rogers Department of Electrical
and Computer Engineering
University of Toronto
Toronto, Ontario M5S 3G4, Canada
E-mail: ted.sargent@utoronto.ca
C. Zhou
Key Laboratory of Materials for High-Power Laser
Shanghai Institute of Optics and Fine Mechanics
Chinese Academy of Sciences
Shanghai 201800, China

[+]Present address: Department of Chemistry and Electrical and Computer Engineering, Centre for Advanced Materials and Related Technologies (CAMTEC), University of Victoria, Victoria, British Columbia V8P 5C2, Canada

lasing are limited to nanowires[12,13] and microcubes[14,15] which have inherent device integration problems. This gap is largely because of thin-film synthesis difficulties and energetically favorable deep traps in wide-bandgap semiconductors: on the one hand, low solubility of chloride-based precursors[16] aggravates the fabrication of films which are essential for cavity integration; on the other hand, chloride vacancies introduce trap states within the bandgap[17] leading to increased nonradiative recombination rates and overall low photoluminescence quantum yields (PLQYs).

In this work, we demonstrate room-temperature single-mode deep-blue ASE and lasing using $(BA)_2Cs_{n-1}Pb_nCl_{3n+1}$. The low solubility of chloride-based precursors relative to bromide and iodide counterparts leads to lower film quality. To overcome this difficulty, we developed an efficient vapor-assisted postsynthesis chlorination procedure to fully convert high-quality green-emitting $(BA)_2Cs_{n-1}Pb_nBr_{3n+1}$ into chloride-based perovskite films with a surface roughness of less than 1.5 nm (root-mean-square, RMS), efficient charge transfer, and low-threshold ASE. A vertical-cavity surface-emitting laser (VCSEL) consisting of two distributed Bragg reflectors (DBRs) and a high-quality $(BA)_2Cs_5Pb_6Cl_{19}$ film is fabricated to achieve deep-blue (425 nm) room-temperature single-mode lasing with a threshold of 6.5 μJ cm^{-2}.

Previous works on green and red-emitting RDPs were based on the small monovalent $CH_3NH_3^+$ (MA$^+$) occupying the A cation position in the perovskite structure.[3,4,11] However, MA-BX$_3$ single crystals, polycrystalline films, and

quantum-confined structures showed outstanding performances only within the green- and red-emitting spectral range (with bromide and iodide occupying the halide position). Room temperature stimulated emission in the form of lasing or ASE was not achieved with MAPbCl$_3$, presumably owing to the high trap density in this material.[18,19] As such, cesium (Cs) was chosen to occupy the A-site position of the perovskite structure. A larger organic cation, such as butylammonium (BA, $C_4H_9NH_3^+$), is used to bisect the 3D perovskite lattice along one axis to form $(BA)_2Cs_{n-1}Pb_nCl_{3n-1}$. The low solubility in dimethylsulfoxide (DMSO) of chloride-based precursors relative to bromide and iodide counterparts is shown in **Figure 1a**. Other commonly used organic solvents such as dimethylformamide (DMF) and γ-butyrolactone (GBL) reached saturation with even lower precursor concentrations. The maximum achievable chloride-based precursor solution concentration (which includes BACl, PbCl$_2$, and CsCl) is limited by the solubility of CsCl, of ≈0.07 M in DMSO.

The standard approach for bromide-based and iodide-based perovskite film fabrication relies on spin-coating, with an intermediate antisolvent dripping step which leads to perovskite crystallization (Figure S1, Supporting Information). The same technique applied to chloride-based perovskites leads to high surface roughness (RMS ≈ 7.6 nm) and high peak-to-valley height variations of the perovskite film (Figure 1b). Because of the low solubility of the precursors, little can be dissolved before reaching solvent saturation. The subsequent evaporation of the saturated solvent during the spinning step leads
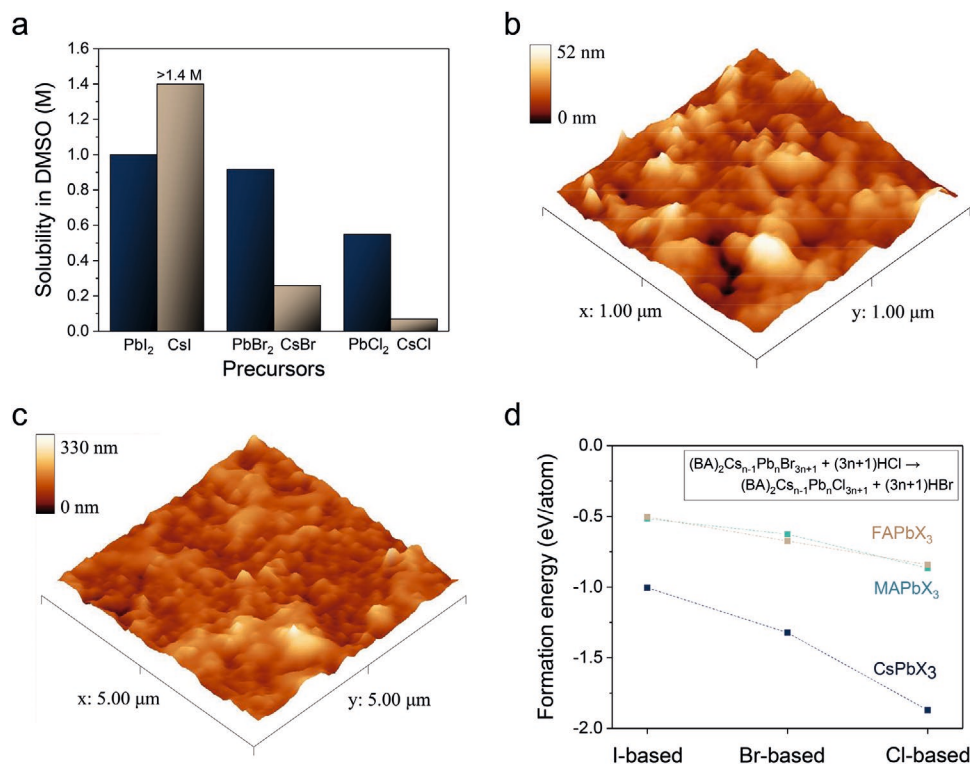

Figure 1. Chloride-based films synthesized using previously reported methods. a) Solubility of inorganic iodide, bromide, and chloride precursors in DMSO. b) AFM height image of $(BA)_2Cs_5Pb_6Cl_{19}$ film using one-step synthesis method (RMS ≈ 7.6 nm). c) AFM height image of $(BA)_2Cs_5Pb_6Cl_{19}$ film using a two-step synthesis method (RMS ≈ 36.2 nm). d) Formation energy calculations for iodide, bromide, and chloride-based perovskites. The inset shows the chemical equation of the halide exchange reaction of $(BA)_2Cs_{n-1}Pb_nBr_{3n+1}$ to $(BA)_2Cs_{n-1}Pb_nCl_{3n+1}$.

to unwanted precursor precipitation and perovskite formation. Other film fabrication methodologies, such as a two-step approach (Figure S2, Supporting Information), led to equally large surface roughness and peak-to-valley height variation (Figure 1c). This method often leads to large grain sizes[20–22] which increase optical propagation losses because of scattering at the grain boundaries.

To circumvent the difficulties in synthesizing high-quality chloride-based perovskite films, other approaches were considered. Chloride-based perovskites have the lowest formation energy compared to their bromide and iodide counterparts, a trend that is especially evident in $CsPbX_3$ (Figure 1d). We hypothesized that if a bromide-based perovskite film is synthesized, the significantly lower formation energy of chloride-based perovskites would allow for an efficient halide exchange (bromide for chloride) process when in contact with a chloride source such as HCl (following the chemical reaction shown in the inset of Figure 1d). Furthermore, as the building blocks composing the perovskite are already in place, exchanging

chlorides for bromides would not diminish the surface quality of the film. Halide exchange in perovskite nanocrystals has been previously demonstrated.[23,24] Less extensively studied is halide exchange in presynthesized polycrystalline films, where prior methods have come at the cost of a large surface roughness and poor optoelectronic properties.[25,26]

Hydrochloric acid (HCl, 12 м) is bubbled using N_2 or argon as a carrier gas through the sample chamber (**Figure 2**a). Prior to reaching the sample chamber, the vapor is passed through a desiccation chamber to remove most of the water content of the gas; moisture is shown to diminish film morphology and optical properties of the synthesized film. Halide exchange was not achieved in 2D perovskites (Figure S3, Supporting Information), whereas with the presence of inorganic cesium, partial and complete anion exchange are achieved in RDPs. In contrast with prior reports, the exchange process is carried out at room temperature and does not require further annealing. This is because of the favorable low-formation energy of chloride-based perovskites. Figure 2b shows the absorption spectra variation
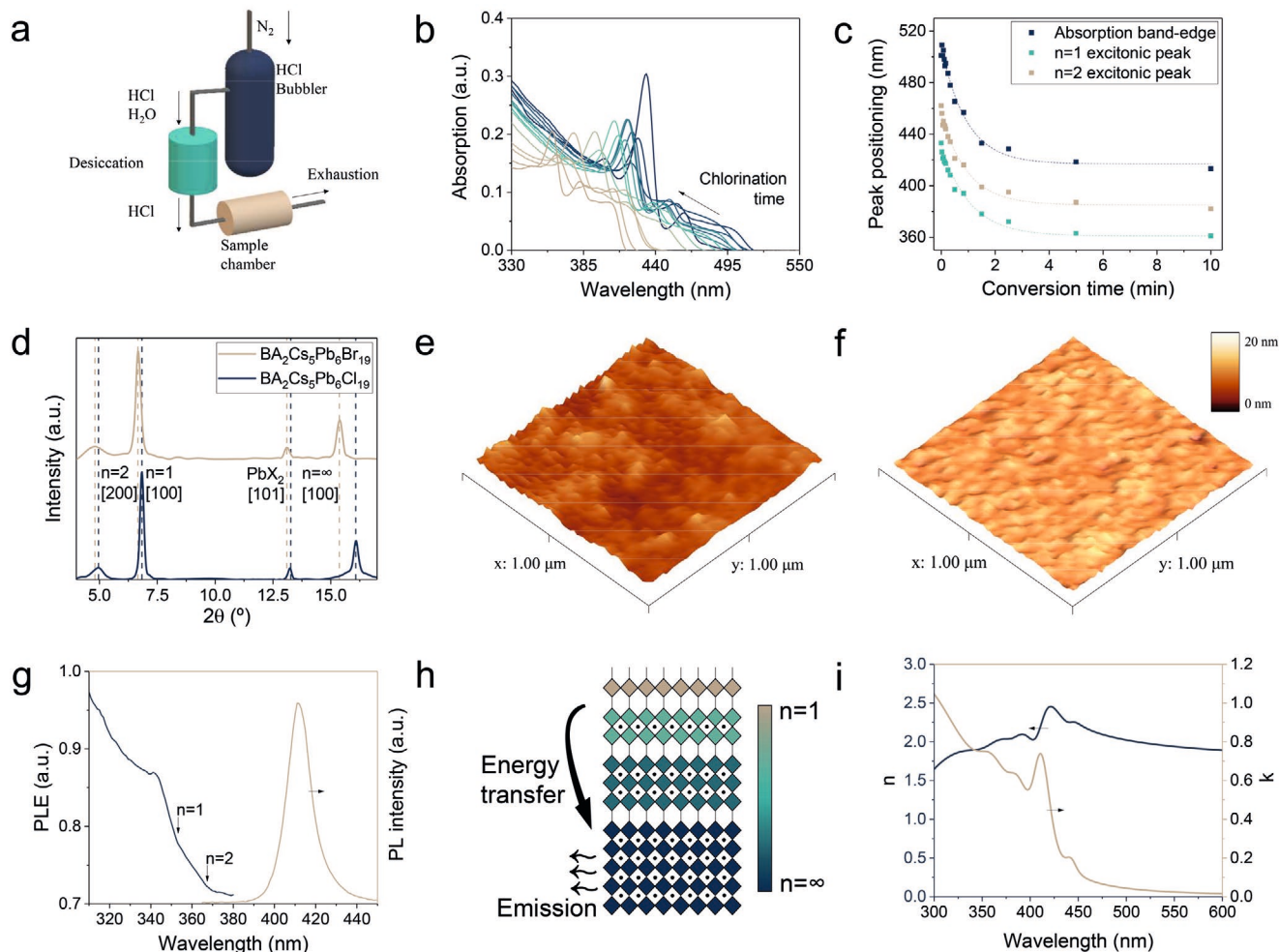

Figure 2. Vapor-assisted chlorination for the fabrication of high-quality blue-emitting films. a) Schematic of the setup used for vapor-assisted chlorination. b) Absorption profile variation as a function of the chlorination time. c) Wavelength position of $n = 1$ and $n = 2$ excitonic peaks and 3D absorption edge as a function of chlorination time. d) XRD peaks before and after the chlorination process. e,f) AFM height image of a bromide-based perovskite film before (RMS ≈ 1.8 nm) and after the chlorination process (RMS ≈ 1.3 nm). g) PLE and PL of a fully converted film showing emission at 415 nm. h) Schematic of the energy transfer process within layered perovskites toward smaller-bandgap domains. i) Optical constants obtained by ellipsometry.

**ADVANCED
SCIENCE NEWS** _____
www.advancedsciencenews.com

**ADVANCED
MATERIALS**
www.advmat.de

with increasing chlorination time. The excitonic peaks corresponding to $n = 1$ and $n = 2$ quantum wells and the band edge correspondent to the 3D domains of the material blueshift from a full-bromide perovskite to the position expected for a full-chloride perovskite (Figure 2c). The final peaks are ≈100 nm blueshifted from the initial bromide film, demonstrating an efficient exchange process. X-ray diffraction (XRD) peaks corresponding to $n = 1$ [100], $n = 2$ [200], and $n = \infty$ (3D domain) [100] obtained after chlorination show a clear shift toward higher angles (Figure 2d), consistent with the smaller lattice constant of chloride-based perovskites.

For a stoichiometry of $\langle n \rangle = 6$, high-quality green-emitting films synthesized using a standard methodology (Figure S1, Supporting Information) are obtained with RMS ≈ 1.8 nm and peak-to-valley height variations below 20 nm (Figure 2e). In contrast to directly synthesized chloride-based films (Figure 1b,c), through vapor-assisted chlorination of bromide-based perovskites, a fully chloride perovskite film can be obtained with RMS ≈ 1.3 nm (Figure 2f). The surface morphology improvement is attributed to the chlorination process which isotropically etches the surface roughness features of the film (Figure S4, Supporting Information). Figure 2g shows a photoluminescence excitation (PLE) and photoluminescence (PL) spectra of the fully converted film showing emission at around 410 nm. The PLE spectrum shows an increased rate emission at excitation wavelengths lower than 370 and 355 nm, corresponding to the position of the $n = 2$ and $n = 1$ excitonic peak, respectively. The increased photoluminescence intensity as a function of the excitation wavelength with a well-defined

single emission peak demonstrates the efficient charge transfer mechanism between quantum wells with various n values. Figure 2h shows a schematic of the transfer mechanism with carrier funneling from large bandgap (highly confined) to lower bandgap domains. The real and imaginary parts of the dielectric function (Figure 2i) show several features corresponding to the differently sized wells. The high refractive index within the wavelength range of light emission ($n \approx 2.4$) suggests that substantial modal confinement can be achieved with RDPs thin films. This is an advantage over other solution-based quantum-confined structures such as quantum dots, whose refractive index is $n \approx 2$.[27,28]

By controlling the anionic stoichiometry through means of chlorination time, the ASE peak position can be tuned within a range of 100 nm (**Figure 3**a). Images of the films used for ASE measurements are shown in Figure S5 (Supporting Information). We optimized the initial synthesis conditions and stoichiometry of bromide-based films to achieve a green-emitting ASE threshold of 7.2 μJ cm^{-2}, as shown in Figure 3b.

The deep-blue ASE spectra and power-dependent PL of the films after chlorination are shown in Figure 3c. As expected, the threshold is increased in comparison with the green-emitting perovskite films. Because of the increased bandgap of chloride perovskites in comparison with bromide and iodide counterparts, halogen vacancies lead to trap states occupying deeper energies within the bandgap, therefore increasing the rate of nonradiative recombination.[17] Furthermore, the chlorination process reduces the film thickness by a factor of 2 (Figure S6, Supporting Information). This decreases the
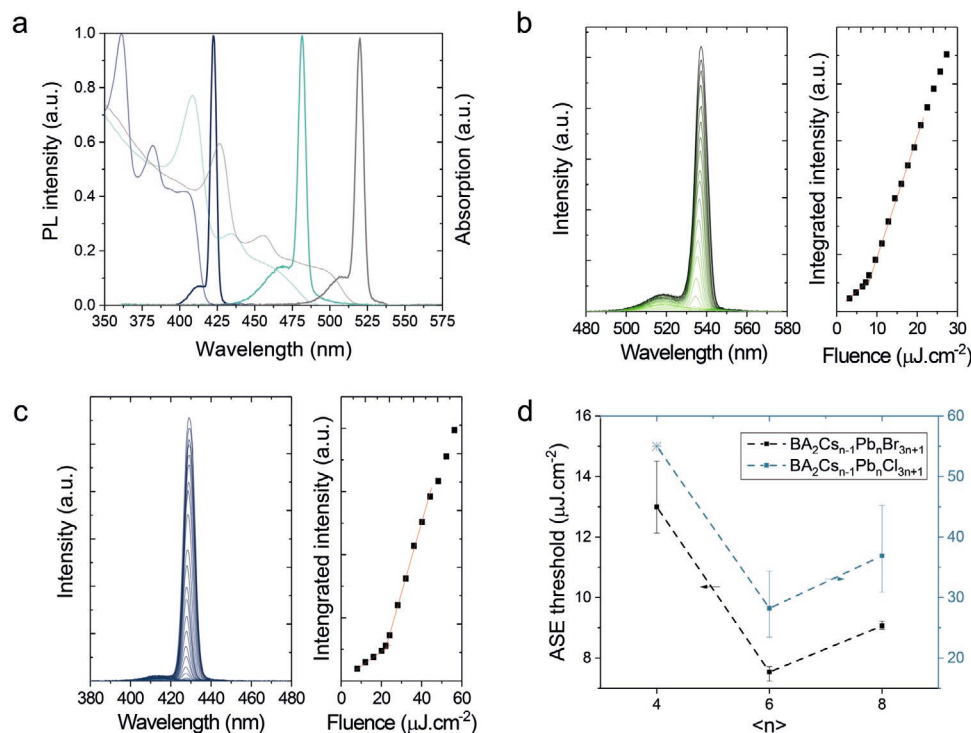

Figure 3. Amplified spontaneous emission from 250 fs pulsed excitation in perovskite films before and after the vapor-assisted chlorination process. a) Wavelength tunability of ASE controlled by chlorination time. b,c) ASE spectra and power-dependent PL of an $\langle n \rangle = 6$ perovskite film before and after halide exchange. d) ASE threshold comparison before ((BA)$_2$Cs$_{n-1}$Pb$_n$Br$_{3n+1}$) and after ((BA)$_2$Cs$_{n-1}$Pb$_n$Cl$_{3n+1}$) halide exchange for different average n values.

modal confinement of emitted light by ≈20% which further increases the ASE threshold (Figure S7, Supporting Information). Consistent with previous green-emitting RDPs reports,[4] the lowest achieved ASE threshold is obtained for a stoichiometry of $\langle n \rangle = 6$. The curved profile of Figure 3d demonstrates that precise control of stoichiometry is required to achieve low-threshold ASE. A 3D perovskite ($n = \infty$) has high modal gain; however, it can be improved in an RDP form because of the improved film morphology and faster population inversion via energy transfer along quantum wells. In the limit of $n = 1$ (2D perovskite), stimulated emission is not achieved because of strong electron–phonon interactions which provide the required momentum for band edge-to-trap processes,[29] leading to free exciton trapping and bound biexciton formation pathways that effectively compete with biexcitonic gain.[30] This leads to a higher ASE threshold for $\langle n \rangle = 4$ green-emitting perovskites, and no ASE was obtained after the chlorination process.

A vertical-cavity surface-emitting laser was built using a 70 nm $(BA)_2Cs_5Pb_6Cl_{19}$ film placed between two high-reflectivity (>99.8%) DBR mirrors, as shown in **Figure 4**a. The DBR transmission spectrum (Figure 4b) shows a stop band which encloses the emission wavelength of the film. The excitation wavelength was set to 337 nm which falls into a high transmission fringe of the DBR. Excitation was applied normal to the bottom DBR mirror, and the emission was collected normal to the top DBR mirror (Figure S8, Supporting Information). Figure 4c shows the PL spectra at different pump fluences. Room-temperature

single-mode lasing is achieved with a full-width half-maximum (FWHM) of 1.35 nm (Figure 4d). This is an upper-bound value as it is limited by the spectrometer resolution, but represents a clear reduction relative to the SE FWHM (≈13 nm). Power-dependent PL (Figure 4e) shows a clear threshold at around 6.5 µJ cm^{-2} followed by an output-power increase of two to three orders of magnitude. Below threshold, broader PL because of spontaneous emission is obtained (Figure S9, Supporting Information). An image of the transparent device is shown in Figure S10 (Supporting Information). One property of lasing is that the emission wavelength will be characteristic of the specific gain medium and resonator cavity length.[31] By slightly misaligning the position of the top DBR with respect to the bottom DBR, therefore changing the path-length between the mirrors, resonances centered at different wavelengths are obtained, showing that the lasing wavelength can be tuned with cavity length. This is shown in Figure S11 (Supporting Information). This helps to differentiate ASE from true laser operation as ASE is not influenced by the resonator characteristics.[31]

In summary, thin-film deep-blue amplified spontaneous emission and single-mode lasing are achieved at room temperature in perovskites for the first time. We found that vapor-assisted chlorination of green-emitting bromide-based perovskite films is a viable route toward high-quality fully chloride-based perovskite films. This strategy circumvents the difficulties in producing high-quality chloride-based films because of the inherent low solubility of the precursors. Films of $(BA)_2Cs_5Pb_6Cl_{19}$ suitable for cavity integration (RMS ≈ 1.3 nm)

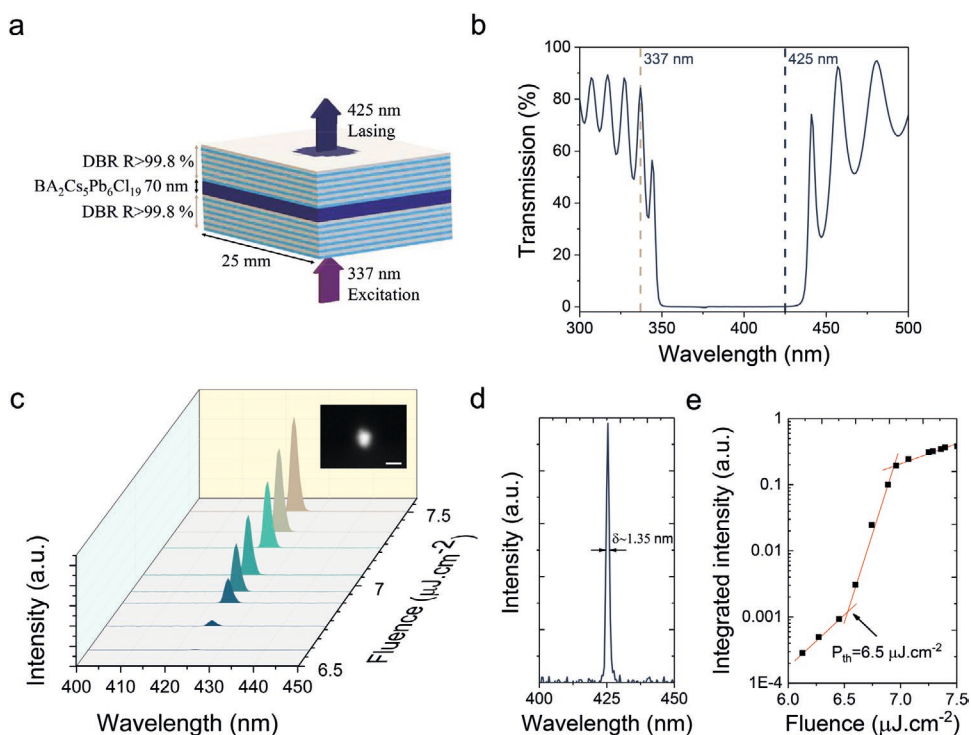**Figure 4.** Low-threshold lasing from 250 fs pulsed excitation using a VCSEL structure. a) Schematic of the $(BA)_2Cs_5Pb_6Cl_{19}$ VCSEL. b) Transmission spectrum of the DBR mirror: excitation and lasing wavelengths are shown with a dashed line. c) Power-dependent emission spectra from the perovskite VCSEL. The inset shows a far-field image of the device's emission with pumping intensity above the lasing threshold (scale bar: 500 µm). d) Lasing spectra with reduced FWHM (limited by spectrometer resolution). e) Integrated power-dependent PL as a function of excitation fluence, showing a lasing threshold of 6.5 µJ cm^{-2}.

were used to fabricate a vertical-cavity surface-emitting laser. Low-threshold (6.5 µJ cm^{-2}) single-mode lasing was achieved at room temperature in ambient conditions showing the feasibility of the proposed approach.

Experimental Section

Materials and Chemicals: Cesium bromide (CsBr), lead bromide (PbBr$_2$), and DMSO were purchased from Sigma-Aldrich. Butylammonium bromide (BABr) was purchased from GreatCell Solar. Chloroform was purchased from DriSolv. Hydrochloric acid (HCl) (37%) was purchased from Caledon Laboratory Chemicals. All chemicals were used as received.

Bromide-Based RDP Thin-Film Fabrication: The precursor solution was prepared by dissolving stoichiometric quantities of PbBr$_2$ (0.5 м), CsBr and BABr in DMSO under continuous stirring for 1h at room temperature. Glass substrates were O$_2$ plasma-treated to improve adhesion. The precursor solution was spin-coated onto the substrates via a two-step process: 1000 rpm for 10 s and 5000 rpm for 60 s. During the second spin step, 1 mL of chloroform was poured onto the substrate. The films were then annealed at 95 °C for 7.5 min. All the samples were prepared in a glove box with N$_2$ atmosphere to control the atmospheric conditions; however, similar results were obtained when the preparation was done under ambient conditions.

Chloride-Based RDP Thin-Film Fabrication: Bromide-based RDP films were introduced into the sample chamber in a home-built vapor transport system. HCl was bubbled using N$_2$ or argon through the sample chamber (of ≈90 cm^3). The vapor is passed through a desiccation chamber to remove most of the water content of the gas. Conversion time was dependent on the degradation state of the HCl and gas flow.

VCSEL Fabrication: Two commercially available DBRs (*R*[0°, 370–425 nm] > 99.8%) were purchased from LayerTec Optical Coating. A bromide-based RDP thin film was spun onto one DBR according to the procedure described in the section Bromide-Based RDP Thin-Film Fabrication. Further on, the bromide-based film was halide exchanged using the procedure described in the section Chloride-Based RDP Thin-Film Fabrication. The two DBRs were then aligned using the optical setup shown in Figure S8 (Supporting Information).

Structural Characterizations: X-ray diffractograms were recorded using a Rigaku MiniFlex 600 powder X-ray diffractometer equipped with a NaI scintillation counter and using monochromatized Cu Kα radiation (*l* = 1.5406 Å).

Optical Measurements: UV–vis absorption was measured using a Perkin Elmer LAMBDA 950 UV–vis–NIR spectrometer; in the measurement, light is transmitted through the film, thus simultaneously providing absorption contributions of the surface and the interior of the film. PL and PLE spectra were recorded using a Horiba Fluorolog system using a Xe lamp as the excitation source. Ellipsometry measurements were performed using Horiba Jobin Yvon UVISEL Ellipsometer. The obtained data were fitted using DeltaPsi2. The films were treated as substrates with optical constants defined by a Kramers–Kronig consistent series of Voigt oscillators.

ASE and Lasing Measurements: Samples were optically excited using a 340 nm (337 nm for lasing measurements) femtosecond laser source with a repetition rate of 1000 Hz. The laser source consisted of a Yb:KGW regenerative amplifier (Pharos, Light Conversion) with 1030 nm fundamental which is passed through an optical parametric amplifier (Orpheus, Light Conversion) to generate the 340 nm pump light pulse. The spectral data were collected using a UV–vis USB 2000+ spectrometer (Ocean Optics). A multimode fiber was used to collect all spectral data, except for the data presented in Figure 4d, which were collected with a single-mode fiber allowing a maximum resolution of ≈1.4 nm. During laser characterization measurements, because of the low photon fluence available below threshold, three measurements per fluence were acquired, and only the fluence datapoints with the same integrated intensity were used.

Atomic Force Microscopy (AFM) Measurements: Surface morphology was characterized using an Asylum Research Cypher operating in tapping mode. The data were analyzed using WSxM software.[32]

First-Principle Calculations: Formation energies were obtained using first-principle density functional theory (DFT) calculations. Using Perdew–Burke–Ernzerhof (PBE) functional as implemented in VASP, total energies of the systems were calculated on a k-points grid of size 3 × 3 × 2 and centered at gamma. Formation energies were further calculated with respect to standard states of constituent elements which were then normalized to formation energy per atom. Pymatgen[33] phase diagram was used to query Materials Project[34] database to first benchmark the obtained formation energy results for MAPbI$_3$. With consistent benchmarking settings, the formation energies were calculated for the rest of the compositions.

Supporting Information

Acknowledgements

Conflict of Interest

The authors declare no conflict of interest.

Keywords

[1] L. A. Coldren, S. W. Corzine, M. L. Mashanovitch, *Diode Lasers and Photonic Integrated Circuits*, 2nd ed., Wiley, New York **2012**.

[2] H. C. Casey, M. B. Panish, *Heterostructure Lasers*, Academic, New York **1978**.

[3] M. Li, Q. Wei, S. K. Muduli, N. Yantara, Q. Xu, N. Mathews, S. G. Mhaisalkar, G. Xing, T. C. Sum, *Adv. Mater.* **2018**, *30*, 1707235.

[4] H. Zhang, Q. Liao, Y. Wu, Z. Zhang, Q. Gao, P. Liu, M. Li, J. Yao, H. Fu, *Adv. Mater.* **2018**, *30*, 1706186.

[5] M. Li, Q. Gao, P. Liu, Q. Liao, H. Zhang, J. Yao, W. Hu, Y. Wu, H. Fu, *Adv. Funct. Mater.* **2018**, *28*, 1707006.

[6] X. Hong, T. Ishihara, A. V. Nurmikko, *Phys. Rev. B* **1992**, *45*, 6961.

[7] J. Xing, Y. Zhao, M. Askerka, L. N. Quan, X. Gong, W. Zhao, J. Zhao, H. Tan, G. Long, L. Gao, Z. Yang, O. Voznyy, J. Tang, Z.-H. Lu, Q. Xiong, E. H. Sargent, *Nat. Commun.* **2018**, *9*, 3541.

[8] G. Xing, B. Wu, X. Wu, M. Li, B. Du, Q. Wei, J. Guo, E. K. L. Yeow, T. C. Sum, W. Huang, *Nat. Commun.* **2017**, *8*, 14558.

**ADVANCED
SCIENCE NEWS**

www.advancedsciencenews.com

**ADVANCED
MATERIALS**

www.advmat.de

[9] H. Zheng, G. Liu, L. Zhu, J. Ye, X. Zhang, A. Alsaedi, T. Hayat, X. Pan, S. Dai, *Adv. Energy Mater.* **2018**, *8*, 1800051.

[10] J. Guo, T. Liu, M. Li, C. Liang, K. Wang, G. Hong, Y. Tang, G. Long, S.-F. Yu, T.-W. Lee, W. Huang, G. Xing, *Nat. Commun.* **2020**, *11*, 3361.

[11] M. R. Leyden, T. Matsushima, C. Qin, S. Ruan, H. Ye, C. Adachi, *Phys. Chem. Chem. Phys.* **2018**, *20*, 15030.

[12] Y. Fu, H. Zhu, C. C. Stoumpos, Q. Ding, J. Wang, M. G. Kanatzidis, X. Zhu, S. Jin, *ACS Nano* **2016**, *10*, 7963.

[13] S. W. Eaton, M. Lai, N. A. Gibson, A. B. Wong, L. Dou, J. Ma, L.-W. Wang, S. R. Leone, P. Yang, *Proc. Natl. Acad. Sci. USA* **2016**, *113*, 1993.

[14] Z. Hu, Z. Liu, Y. Bian, D. Liu, X. Tang, W. Hu, Z. Zang, M. Zhou, L. Sun, J. Tang, Y. Li, J. Du, Y. Leng, *Adv. Opt. Mater.* **2017**, *5*, 1700419.

[15] X. He, P. Liu, H. Zhang, Q. Liao, J. Yao, H. Fu, *Adv. Mater.* **2017**, *29*, 1604510.

[16] H. Wang, X. Zhao, B. Zhang, Z. Xie, *J. Mater. Chem. C* **2019**, *7*, 5596.

[17] A. Buin, R. Comin, J. Xu, A. H. Ip, E. H. Sargent, *Chem. Mater.* **2015**, *27*, 4405.

[18] G. Xing, N. Mathews, S. S. Lim, N. Yantara, X. Liu, D. Sabba, M. Grätzel, S. Mhaisalkar, T. C. Sum, *Nat. Mater.* **2014**, *13*, 476.

[19] H. Zhu, Y. Fu, F. Meng, X. Wu, Z. Gong, Q. Ding, M. V. Gustafsson, M. T. Trinh, S. Jin, X.-Y. Zhu, *Nat. Mater.* **2015**, *14*, 636.

[20] A. Bahtiar, S. Rahmanita, Y. D. Inayatie, *IOP Conf. Ser.: Mater. Sci. Eng.* **2017**, *196*, 012037.

[21] K. Liang, D. B. Mitzi, M. T. Prikas, *Chem. Mater.* **1998**, *10*, 403.

[22] B. R. Sutherland, S. Hoogland, M. M. Adachi, C. T. O. Wong, E. H. Sargent, *ACS Nano* **2014**, *8*, 10947.

[23] G. Nedelcu, L. Protesescu, S. Yakunin, M. I. Bodnarchuk, M. J. Grotevent, M. V. Kovalenko, *Nano Lett.* **2015**, *15*, 5635.

[24] Q. A. Akkerman, V. D'Innocenzo, S. Accornero, A. Scarpellini, A. Petrozza, M. Prato, L. Manna, *J. Am. Chem. Soc.* **2015**, *137*, 10276.

[25] S. E. Creutz, E. N. Crites, M. C. D. Siena, D. R. Gamelin, *Chem. Mater.* **2018**, *30*, 4887.

[26] A. Pushkarev, V. Korolev, S. Anoshkin, F. Komissarenko, S. Makarov, A. Zakhidov, *J. Phys.: Conf. Ser.* **2018**, *1092*, 012122.

[27] M. M. Adachi, F. Fan, D. P. Sellan, S. Hoogland, O. Voznyy, A. J. Houtepen, K. D. Parrish, P. Kanjanaboos, J. A. Malen, E. H. Sargent, *Nat. Commun.* **2015**, *6*, 8694.

[28] J. Roh, Y.-S. Park, J. Lim, V. I. Klimov, *Nat. Commun.* **2020**, *11*, 271.

[29] X. Gong, O. Voznyy, A. Jain, W. Liu, R. Sabatini, Z. Piontkowski, G. Walters, G. Bappi, S. Nokhrin, O. Bushuyev, M. Yuan, R. Comin, D. Mccamant, S. O. Kelley, E. H. Sargent, *Nat. Mater.* **2018**, *17*, 550.

[30] W. K. Chong, K. Thirumal, D. Giovanni, T. W. Goh, X. Liu, N. Mathews, S. Mhaisalkar, T. C. Sum, *Phys. Chem. Chem. Phys.* **2016**, *18*, 14701.

[31] I. D. W. Samuel, E. B. Namdas, G. A. Turnbull, *Nat. Photonics* **2009**, *3*, 546.

[32] I. Horcas, R. Fernández, J. M. Gómez-Rodríguez, J. Colchero, J. Gómez-Herrero, A. M. Baro, *Rev. Sci. Instrum.* **2007**, *78*, 013705.

[33] S. P. Ong, W. D. Richards, A. Jain, G. Hautier, M. Kocher, S. Cholia, D. Gunter, V. L. Chevrier, K. A. Persson, G. Ceder, *Comput. Mater. Sci.* **2013**, *68*, 314.

[34] A. Jain, S. P. Ong, G. Hautier, W. Chen, W. D. Richards, S. Dacek, S. Cholia, D. Gunter, D. Skinner, G. Ceder, K. A. Persson, *APL Mater.* **2013**, *1*, 011002.